PHOTONICS Research

Chiral forces in longitudinally invariant dielectric photonic waveguides

Josep Martínez-Romeu,[1,†] Iago Diez,[1,†] Sebastian Golat,[2] Francisco J. Rodríguez-Fortuño,[2] and Alejandro Martínez[1,*]

[1]Nanophotonics Technology Center, Universitat Politècnica de València, Valencia 46022, Spain
[2]Department of Physics, King's College London, London WC2R 2LS, UK
[†]These authors contributed equally to this work.
[*]Corresponding author: amartinez@ntc.upv.es

We calculate numerically the optical chiral forces in rectangular cross-section dielectric waveguides for potential enantiomer separation. Our study considers force strength and time needed for separating chiral nanoparticles, mainly via quasi-TE guided modes at short wavelengths (405 nm) and the 90°-phase-shifted combination of quasi-TE and quasi-TM modes at longer wavelengths (1310 nm). Particle tracking simulations show successful enantiomer separation within two seconds. These results suggest the feasibility of enantiomeric separation of nanoparticles displaying sufficient chirality using simple silicon photonic integrated circuits, with wavelength selection based on the nanoparticle size.   © 2024 Chinese Laser Press

https://doi.org/10.1364/PRJ.509634

1. INTRODUCTION

Separation of enantiomers from racemic mixtures is essential in fields such as chemistry and pharmaceutics since the required performance is only exhibited by an enantiomer with a certain handedness (or chirality). Usually, methods based on chemical interactions, such as chiral high-performance liquid chromatography (HPLC), are employed to separate enantiomers starting from racemic mixtures. However, such chemical methods are usually slow, expensive, and molecule-dependent [1]. An interesting alternative would be the use of optical chiral forces [2]: since the chiral force exerted by light changes its sign when acting on enantiomers of different handedness [3], it could ultimately lead to light-driven enantiomeric separation overcoming many of the limitations of chemical methods.

There have been many recent theoretical and simulation works addressing the separation of enantiomers using light [4–10]. Indeed, there have been several experiments demonstrating optically induced separation, though for relatively large nanoparticles and nanostructures [11–13]. In all cases, free-space propagating beams are used, either being reflected at dielectric interfaces [5] or interfering with other beams [7] to produce the transverse optical spin that generates the required forces. Alternatively, one may think of using guided light for separation purposes, taking advantage of the enhancement of chiral interaction because the light is confined in subwavelength cross-sections over relatively long distances (ideally infinite for a lossless waveguide). One possibility is the use of optical nanofibers with cylindrical cross-sections, as recently noticed by Golat *et al.* [14]. Another possibility would be the use of dielectric waveguides that can be created by lithography in photonic integrated circuits (PICs) and can exhibit either transverse [15] or longitudinal spin [16] for guided modes. Remarkably, such waveguides can be massively integrated into PICs and, in the case of silicon-related materials, fabricated in large volumes using low-cost processes. Recently, several approaches to separate enantiomers using integrated waveguides have been presented [17–19]. However, in all of them, the separating chiral forces are not kept over long propagation distances, just missing this clear advantage of PICs over free-space approaches.

In this work, we analyze the chiral separation properties of the simplest photonic integrated structure: a lossless dielectric waveguide with a rectangular cross-section on a lower-index substrate. We consider silicon nitride (SiN) as the material to build the waveguide core since it is transparent from telecom wavelengths down to the ultraviolet. The refractive index of SiN is large enough to ensure tight guiding when the core lies on a silicon dioxide substrate and is surrounded by water. Remarkably, waveguides with very low propagation loss (<1 dB/cm) can be fabricated using mature tools and processes [20]. We first calculate the order of magnitude of the required chiral forces to perform the enantiomeric separation of particles under a reasonable time assuming Brownian diffusion of the target particles in a liquid environment. Then, we calculate numerically the electric and magnetic fields at different

wavelengths from 405 to 1310 nm to obtain the optical forces using well-established equations [14]. We show that at short wavelengths (405 nm) lateral chiral forces arising from the transversal spin of the guided quasi-TE mode [15] can overcome the achiral forces and be used for separation of chiral particles of 80 nm radius. At longer wavelengths (1310 nm), this lateral force becomes much smaller but we combine the quasi-TE and quasi-TM modes of the waveguide with a proper 90° phase shift between them to generate a quasi-circularly polarized (quasi-CP) mode [16]. This mode produces a large transversal chiral gradient force that could separate nanoparticles of 52 nm radius and potentially molecules with a size of the order of 1 nm. Our results suggest that long SiN waveguides are simple but realistic structures towards achieving enantiomeric separation within seconds using guided light in PICs.

2. OPTICAL FORCES EXERTED ON SMALL CHIRAL PARTICLES

The electromagnetic field of light carries momentum that can be transferred to a particle through the action of an optical force, and consequently, cause its motion. In this work, we restrict to study the motion of small chiral particles (whose size is smaller than the wavelength of light) subjected to optical forces. A small particle is fully characterized by its electric dipole moment, p, which can be thought of as the separation of positive and negative charges, and its magnetic dipole moment, m, which represents the overall current loop within the particle. The time-averaged force F that the electromagnetic field exerts on a small particle is [5,14,21,22]

$$F = \frac{1}{2}\Re\left[\underbrace{(\nabla \otimes E)p^* + \mu(\nabla \otimes H)m^*}_{\text{interaction}} - \underbrace{\frac{k^4\eta}{6\pi}(p^* \times m)}_{\text{recoil}}\right].$$

(1)

In this expression, E and H are, respectively, the electric and the magnetic fields at the position of the particle, $\eta = \sqrt{\mu/\varepsilon}$ is the impedance of the surrounding medium, ε is the electric permittivity of the medium, μ is the magnetic permeability of the medium, $k = 2\pi/\lambda$ is the wavenumber, and λ is the wavelength of light. The dipole moments of a particle arise due to its interaction with the electric and magnetic fields of light, and are obtained as follows:

$$p = \alpha_e \varepsilon E + i\frac{1}{c}\alpha_c H,$$

$$m = \alpha_m H - i\frac{1}{\eta}\alpha_c E,$$

(2)

where $(\alpha_e, \alpha_m, \alpha_c)$ are the dynamic electric, magnetic, and chiral polarizabilities of the particle, and $c = 1/\sqrt{\mu\varepsilon}$ is the speed of light in the medium. The static polarizabilities of a spherical particle of radius r can be modeled using the generalized Clausius-Mossotti expressions [2,6]

$$\alpha_{0e} = 4\pi r^3 \frac{(\varepsilon_p - \varepsilon_m)(\mu_p + 2\mu_m) - \kappa^2}{(\varepsilon_p + 2\varepsilon_m)(\mu_p + 2\mu_m) - \kappa^2},$$

$$\alpha_{0m} = 4\pi r^3 \frac{(\varepsilon_p + 2\varepsilon_m)(\mu_p - \mu_m) - \kappa^2}{(\varepsilon_p + 2\varepsilon_m)(\mu_p + 2\mu_m) - \kappa^2},$$

$$\alpha_{0c} = 12\pi r^3 \frac{\kappa}{(\varepsilon_p + 2\varepsilon_m)(\mu_p + 2\mu_m) - \kappa^2},$$

(3)

where $(\varepsilon_p, \mu_p, \kappa)$ refer to the relative permittivity, relative permeability, and chirality parameter of the particle as defined by the constitutive relations $D = \varepsilon_0\varepsilon_p E + i\kappa H/c$ and $B = -i\kappa E/c + \mu_0\mu_p H$, and (ε_m, μ_m) refer to the relative permittivity and permeability of the non-chiral background medium. A radiation damping has to be added to the expressions in Eq. (3) to satisfy the conservation of energy [23,24]. This so-called radiative correction is often applied incorrectly in the literature for chiral particles, because it is only applied to the electric and magnetic polarizabilities, thus, neglecting the correction for the chiral polarizability. However, as shown by Belov *et al.* [23] and Sersic *et al.* [24], the tensor radiative correction has to be applied to the full 6 × 6 square polarizability matrices, yielding the following expressions for the dynamic polarizabilities [14], which are used for calculating the dipole moments in Eq. (2):

$$\alpha_e = \frac{\alpha_{0e} - i\frac{k^3}{6\pi}(\alpha_{0c}^2 - \alpha_{0e}\alpha_{0m})}{1 + \left(\frac{k^3}{6\pi}\right)^2(\alpha_{0c}^2 - \alpha_{0e}\alpha_{0m}) - i\frac{k^3}{6\pi}(\alpha_{0e} + \alpha_{0m})},$$

$$\alpha_m = \frac{\alpha_{0m} - i\frac{k^3}{6\pi}(\alpha_{0c}^2 - \alpha_{0e}\alpha_{0m})}{1 + \left(\frac{k^3}{6\pi}\right)^2(\alpha_{0c}^2 - \alpha_{0e}\alpha_{0m}) - i\frac{k^3}{6\pi}(\alpha_{0e} + \alpha_{0m})},$$

$$\alpha_c = \frac{\alpha_{0c}}{1 + \left(\frac{k^3}{6\pi}\right)^2(\alpha_{0c}^2 - \alpha_{0e}\alpha_{0m}) - i\frac{k^3}{6\pi}(\alpha_{0e} + \alpha_{0m})}.$$

(4)

With Eqs. (1)–(4) we are ready to compute the time-averaged optical force due to a monochromatic electromagnetic field on a small particle. However, we gain more insight by developing the expression of the force from Eq. (1). The force can be split into several terms that depend on the following six time-averaged local field properties: electric energy density W_e, magnetic energy density W_m, helicity density $\mathfrak{G}$, electric spin density S_e, magnetic spin density S_m, and complex Poynting vector $\mathbf{\Pi}$:

$$W_e = \frac{1}{4}\varepsilon|E|^2 \left[\frac{\text{J}}{\text{m}^3}\right],$$

$$W_m = \frac{1}{4}\mu|H|^2 \left[\frac{\text{J}}{\text{m}^3}\right],$$

$$\mathfrak{G} = \frac{1}{2\omega c}\Im(E \cdot H^*) \left[\frac{\text{J} \cdot \text{s}}{\text{m}^3}\right],$$

$$S_e = \frac{1}{4\omega}\Im(\varepsilon E^* \times E) \left[\frac{\text{J} \cdot \text{s}}{\text{m}^3}\right],$$

$$S_m = \frac{1}{4\omega}\Im(\mu H^* \times H) \left[\frac{\text{J} \cdot \text{s}}{\text{m}^3}\right],$$

$$\mathbf{\Pi} = \frac{1}{2}E \times H^* \left[\frac{\text{W}}{\text{m}^2}\right].$$

(5)

The fully developed expression of the optical force acting on a particle is shown below, which has been split into the chiral and achiral terms, depending on whether the terms are a function of the chiral polarizability or not, respectively [14]:

$\mathcal{M}$ is the mobility coefficient of the particle. Under the assumption that the particles have spherical shapes of radius r, the friction coefficient can be expressed as $\gamma = 6\pi\eta r = 1/\mathcal{M}$ (Stoke's law of friction), where η is the dynamic viscosity of the

$$F_{\text{chiral}} = \underbrace{\omega\Re(\alpha_c)\nabla\mathcal{G}}_{\text{helicity gradient}} - \underbrace{\frac{1}{c}\Im(\alpha_c)\nabla\times\Re\Pi}_{\text{vortex}} + \underbrace{\left(2k\Im(\alpha_c) - \frac{k^4}{3\pi}\Re(\alpha_e^*\alpha_c)\right)\omega S_e}_{\text{electric spin}} + \underbrace{\left(2k\Im(\alpha_c) - \frac{k^4}{3\pi}\Re(\alpha_c^*\alpha_m)\right)\omega S_m}_{\text{magnetic spin}},$$

$$F_{\text{achiral}} = \underbrace{\Re(\alpha_e)\nabla W_e}_{\text{electric gradient}} + \underbrace{\Re(\alpha_m)\nabla W_m}_{\text{magnetic gradient}} - \underbrace{\omega\nabla\times(\Im(\alpha_e)S_e + \Im(\alpha_m)S_m)}_{\text{spin–curl}} + \underbrace{\left(\frac{k}{c}\Im(\alpha_e + \alpha_m) - \frac{k^4}{6\pi}\frac{1}{c}(\Re(\alpha_e^*\alpha_m) + |\alpha_c|^2)\right)\Re\Pi}_{\text{radiation pressure}}$$

$$- \underbrace{\frac{k^4}{6\pi}\frac{1}{c}\Im(\alpha_e^*\alpha_m)\Im\Pi}_{\text{flow}},$$

$$\tag{6}$$

where the name for each force term has been taken from the literature [25–27]. All the forces exhibit an inherent dependency on the volume of the particle because the polarizabilities are proportional to r^3. In addition, some of the forces show explicit dependency on the wavelength (or wavenumber) too, being proportional to r^3/λ or r^6/λ^4, such as the electric and magnetic spin forces and radiation pressure force, whereas others, such as the gradient forces, do not. Therefore, the dominance of chiral forces over achiral forces varies depending on particle size and wavelength. A more detailed analysis of the chiral and achiral optical forces exerted on small chiral particles is discussed by Golat *et al.* [14].

3. OPTICALLY DRIVEN MOTION OF SMALL CHIRAL PARTICLES IN A FLUID

To study under what circumstances the optical enantioseparation is possible, we first need to examine the motion of particles in a fluid under the influence of an external chiral optical force field. To this end, we consider the following assumptions for this system: there is no net fluid flow, and the mass of the particles is negligible so that the viscous forces dominate the inertial forces. Under these considerations, the motion of the particle is driven by a combination of the external optical force, F, the friction or drag force due to the viscosity of the fluid (which is opposite to the movement of the particle), and the force arising from the stochastic collisions of the smaller fluid molecules with the particle (Brownian motion). The variation of the particle position, $x(t)$, with time is governed by the overdamped Langevin equation [28–30]

$$0 = \underbrace{-\gamma\frac{dx}{dt}}_{\text{friction}} + \underbrace{F}_{\text{optical}} + \underbrace{\gamma\sqrt{2D}\xi(t)}_{\text{stochastic}}, \tag{7}$$

where $D = k_B T/\gamma = \mathcal{M}k_B T$ is the particle's diffusion coefficient within the bulk of the fluid, k_B is the Boltzmann constant, T is the absolute temperature, γ is the friction coefficient, and

fluid. Equation (7) is a stochastic differential equation that can be solved numerically with the Euler-Maruyama integration scheme to track the location of the particle upon an increment in time Δt [31,32]. The solution can be expressed as

$$x^{(m+1)} = x^{(m)} + \mathcal{M}_{x,\perp}^{(m)}F_x^{(m)}\Delta t + \sqrt{2\mathcal{M}_{x,\perp}^{(m)}k_B T\Delta t}\,N_x(0,1),$$

$$y^{(m+1)} = y^{(m)} + \mathcal{M}_{y,\perp}^{(m)}F_y^{(m)}\Delta t + \sqrt{2\mathcal{M}_{y,\perp}^{(m)}k_B T\Delta t}\,N_y(0,1),$$

$$z^{(m+1)} = z^{(m)} + \mathcal{M}_{z,||}^{(m)}F_z^{(m)}\Delta t + \sqrt{2\mathcal{M}_{z,||}^{(m)}k_B T\Delta t}\,N_z(0,1),$$

$$\tag{8}$$

where the upper index (m) represents the mth instant of time, and $N_{x/y/z}(0,1)$ represent three independent standard normal distributions with 0–mean and 1–variance. The force field $(F_x^{(m)}, F_y^{(m)}, F_z^{(m)})$ and the mobility coefficients are evaluated at the location of the particle $(x^{(m)}, y^{(m)}, z^{(m)})$. The mobility coefficients are modified with respect to their bulk value $\mathcal{M}$ as the particle moves near a boundary, such as the interface of the fluid with the waveguide or the walls of a microfluidic channel. This modification depends on whether the movement of the particle is perpendicular or parallel to the boundary [33]. Equation (8) is used in Section 5 to follow the trajectories of individual particles throughout a microfluidic channel subjected to the force field exerted by the waveguide mode. More details about the equation of motion and modification on the mobilities are given in Appendix A.

The magnitude of the chiral optical forces required for enantiomeric separation and the needed sorting time can be estimated upon further assumptions. For that we examine the movement of a cloud of particles under the influence of an external optical force field in the bulk, i.e., in an infinite system with no boundaries. We followed the derivation from Kravets *et al.* [28]. The enantiomers are modeled as non-interacting spherical particles and are assumed to be initially mixed and distributed within a spherical cloud of diameter L_0, as shown in Fig. 1(a). Let us assume the optical force field is uniform
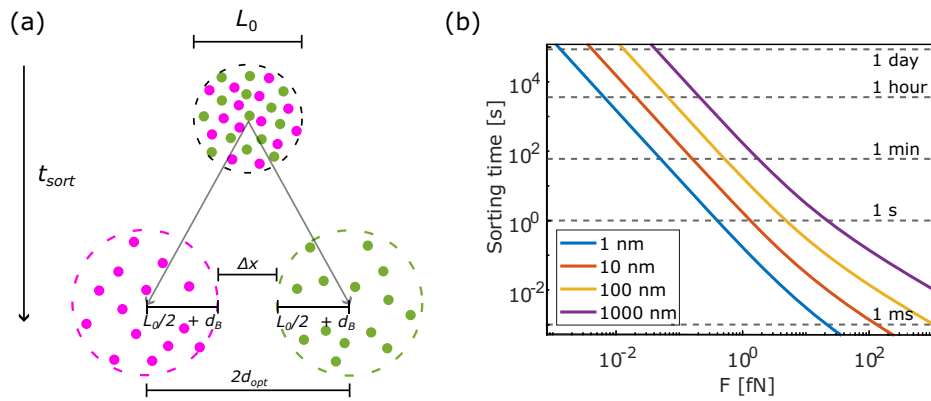
Fig. 1. (a) Schematic showing the combined action of the translation of the cloud of enantiomers due to the optical force (d_{opt}) and the increase in the cloud size due to Brownian motion (d_B). After a sorting time (t_{sort}), the clouds are separated by a distance of Δx. Schematic adapted from Ref. [28]. (b) Sorting time of the enantiomer clouds as a function of the modulus of the separating optical force. Particles of different radii display different sorting time curves, from 1 to 1000 nm.

in space, constant in time, oriented along the x–direction, and dominantly chiral, i.e., the achiral part of the force is negligible compared to the chiral part ($F = |F_{chiral}| \gg |F_{achiral}|$). The chiral optical force F exerted on the particles moves each enantiomer in opposite directions, thus effectively separating the initial racemic mixture into two separate clouds of particles. Upon an interval of time t, each enantiomer cloud is displaced a distance $d_{opt} = Ft/\gamma$ due to the optical force. In addition to this displacement, the radius for each enantiomer cloud is expected to increase on average $d_B = \sqrt{2Dt}$ due to Brownian motion. These two simultaneous processes of motion are schematized in Fig. 1(a). The condition to achieve a separation Δx between the two clouds within a sorting time t_{sort} gives rise to the following equation whose derivation is shown in detail in Appendix B:

$$t_{sort} = 3\pi\eta k_B T \frac{r}{F^2}\left(1 + \sqrt{1 + \frac{F(L_0 + \Delta x)}{k_B T}}\right)^2. \quad (9)$$

In the integrated waveguide system, the particles flow along a microfluidic channel, and the force field is generated by a waveguide. Thus, the actual force field is not spatially uniform and there are boundaries that enclose the region of space where the particles can move and that modify the mobility coefficient value. However, Eq. (9) provides a quite accurate estimation of the sorting time for a longitudinally invariant dielectric waveguide-microchannel system. We assume the initial extension of the racemic mixture cloud is $L_0 = 1$ μm. This is achievable with the well-known microfluidics technique called hydrodynamic flow focusing [34], where two lateral flows can control the width of the middle fluid channel where the particles are suspended. The fluid is composed mainly of water at temperature $T = 293$ K so the dynamic viscosity is $\eta = 10^{-3}$ Pa · s [28].

Figure 1(b) shows the sorting time for particles of different radii, calculated with Eq. (9) for $\Delta x = 0$, which marks the starting point of separation. Stronger forces are needed to sort larger particles for the same value of sorting time. Moreover, larger particles take longer to be sorted for the same value of the force. We emphasize that this sorting time is obtained for a

force field that is constant in time and uniform in space, which is not the actual situation of the force field generated by a waveguide system. In the latter case, the forces are stronger at distances closer to the waveguide and decay with the distance due to the evanescent field of the mode in the fluid. The usefulness of this graph is to know what range of optical force magnitude the waveguide system needs to generate to sort particles under a reasonable time: 1 ms to few hours. We must therefore look for integrated waveguides that generate optical chiral forces within the range of 10^{-3} fN to 10^3 fN for sorting particles of radii between 1 and 1000 nm. Once we have designed those waveguide systems, we use the particle tracking algorithm [Eq. (8)] to test the actual enantiomeric separation that our waveguides can reach.

4. DESCRIPTION OF THE INTEGRATED PHOTONIC WAVEGUIDE

We consider a photonic strip waveguide made with a SiN core (refractive index $n \approx 2$) on top of a SiO$_2$ ($n = 1.4468$) substrate, and surrounded by water ($n = 1.33$) as the system that produces the force field responsible for the enantiomeric sorting, as shown in Fig. 2(a). The use of SiN has several practical advantages such as transparency at visible and near-infrared wavelengths, a relatively large refractive index to ensure tight localization of the fields in the waveguide core, and its processing with a mature silicon technology to produce low-loss waveguides [20]. Moreover, SiN is particularly appropriate for applications requiring immersion in fluid, such as photonic biosensing [35].

In order to obtain the electric and magnetic fields of the guided modes, the Maxwell's equations are solved in the waveguide using the finite element method implemented by the FemSIM solver in the commercial software RSoft (Synopsis). The software computes the eigenmode of the cross-section of the waveguide system, which is assumed to be invariant along the longitudinal direction (translational symmetry along the optical axis, i.e., z–axis). The resulting electric and magnetic fields are plugged into Eq. (6) to obtain the optical forces per amount of power guided by the mode. We assume 20 mW of
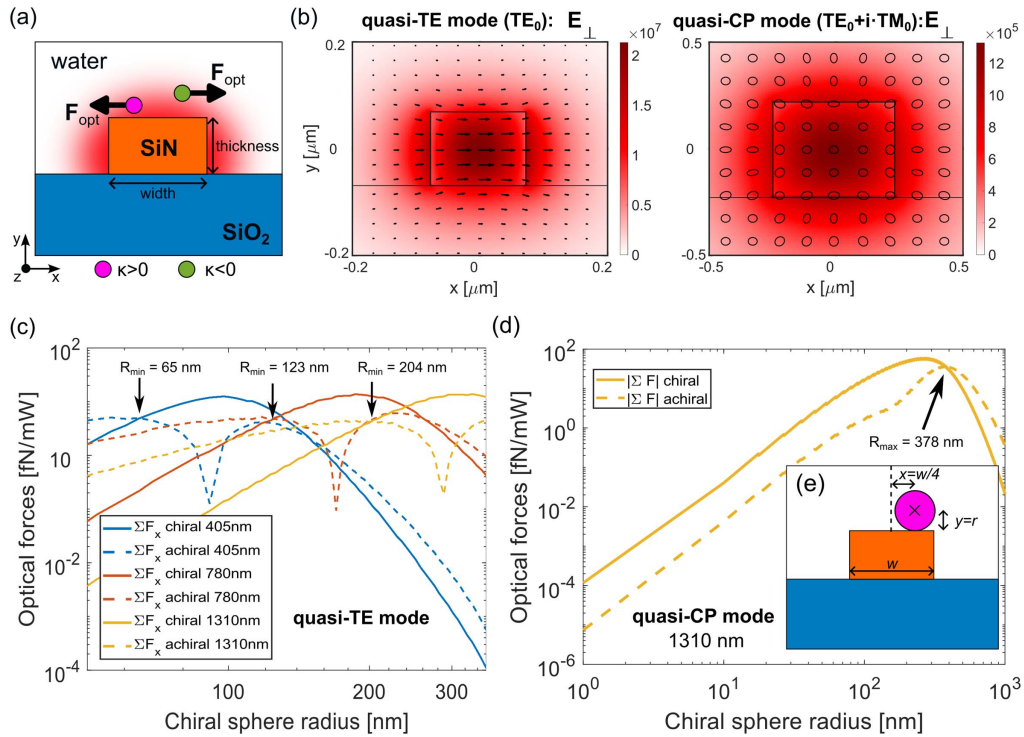
Fig. 2. (a) Schematic of the waveguide cross-section representing the opposite action of the total optical force exerted by the guided mode (in red) onto particles with opposed chirality. (b) Transversal electric field intensity (in color map) and polarization (in arrow or ellipse map) of the quasi-TE mode and of the quasi-CP mode. The handedness of the polarization ellipses does not change its sign throughout the cross-section. (c) Net chiral and achiral force along the x–direction that a quasi-TE mode in a SiN strip waveguide exerts on a particle, depending on its size. This is calculated for three different SiN waveguides, each one operating at a different wavelength: 405 nm, 780 nm, or 1310 nm. The SiN cross-section sizes (width × thickness) of the waveguides are: 0.151 μm × 0.139 μm (for $\lambda = 405$ nm), 0.292 μm × 0.268 μm (for $\lambda = 780$ nm), and 0.495 μm × 0.45 μm (for $\lambda = 1310$ nm). (d) Net transversal chiral and achiral forces that a quasi-CP mode in a strip waveguide exerts on a particle depending on the particle size. (e) Cross-section of the strip waveguide showing the position where the forces are evaluated for (c) and (d): at a vertical distance over the top of the waveguide equal to the radius of the particle, and at a horizontal distance equal to the fourth of the waveguide width from the center of the waveguide. The calculated forces are expected to be more accurate for particles whose size is smaller than the wavelength. This upper bound is ~150 nm, 290 nm, and 490 nm for $\lambda = 405$ nm, 780 nm, and 1310 nm, respectively.

power in our simulations, which, despite being a high power level for integrated optics, can be attained using a standard semiconductor continuous wave laser without causing material damage. Noticeably, the forces depend on the characteristics of the particle, which are modeled by the polarizabilities [Eqs. (3) and (4)]. The particle's material is modeled with a relative permittivity of $\varepsilon_p = 2$, relative permeability $\mu_p = 1$, and chirality parameter $\kappa = \pm 0.5$. These values have been widely used to characterize chiral nanoparticles in the literature [5,36]. The medium (water) is modeled with the values $\varepsilon_m = 1.77$ and $\mu_m = 1$. We take into account the following two design criteria for the waveguide system towards favoring enantiomeric separation: (i) $|F_{\text{chiral}}| > |F_{\text{achiral}}|$, to ensure that chiral forces dominate achiral ones (although it is not a necessary condition for achieving separation); and (ii) $|F_{\text{chiral}}| \sim 10^{-3}$ fN to 10^3 fN, according to our calculations from Fig. 1.

After the total optical force field is computed, we use the particle tracking algorithm to track the position of an individual particle for each enantiomer for 2 s throughout a hypothetical microfluidic channel surrounding the waveguide. Due to the stochastic nature of the Brownian motion, we repeat this tracking 500 times to do a statistical analysis of the

enantioseparation process. In addition, the initial (x, y) positions of the particles were randomized to account for the realistic scenario of not being able to precisely control their starting positions within the microchannel. The initial x–position was uniformly randomized at $x = 0 \pm 0.5$ μm, which is achievable with hydrodynamic flow focusing as commented before [34], and the initial y–position was uniformly randomized throughout the microchannel height. From the final position of the particles we calculate the enantiomer fraction (EF) for each enantiomeric cloud. More details about the particle tracking algorithm and statistical analysis can be found in Appendix A.

5. RESULTS

We consider two different approaches to sorting chiral nanoparticles throughout the transversal plane (xy–plane) around the waveguide: the fundamental quasi-transverse electric mode (quasi-TE mode) for horizontal sorting and a quasi-circularly polarized mode (quasi-CP mode) for attractive-repulsive sorting. The electric field intensity and polarization of the quasi-TE mode and the quasi-CP mode are plotted in Fig. 2(b). A more detailed decomposition of the electric and magnetic fields for

the quasi-TE, quasi-TM, and quasi-CP modes can be found in Appendix C.

A. Quasi-TE Mode

The fundamental quasi-TE mode (or TE_0) in a strip waveguide is characterized by the transverse electric field mainly pointing along the horizontal plane (x–axis) and the transverse magnetic field mainly polarized along the vertical plane (along y–axis). This guided mode exhibits a non-zero longitudinal component of the electric and magnetic fields due to confining the wave inside a waveguide. The longitudinal component oscillates out-of-phase in comparison with the transversal components. This results in a transverse spin [15], which can be interpreted as the quantum spin Hall effect of light [37] and gives rise to transversal chiral forces.

The optical forces that a quasi-TE mode exerts on a particle are computed for a wavelength of 405 nm and a particle radius of 80 nm. The field properties that are responsible for the dominant transversal forces in this system are the electric energy density W_e, the magnetic energy density W_m, and the magnetic spin S_m. These field properties, together with their respective forces, are plotted in Fig. 3. The electric gradient force attracts any particle toward the sidewalls of the waveguide, whereas the magnetic gradient force repels any particle from the top of the waveguide. The magnetic spin force moves the (+)-particles towards the left and the (−)-particles towards the right. Over the top of the waveguide, the achiral gradient electric and gradient magnetic forces have opposite directions, thus reducing the strength of the total achiral force. That is why the chiral force magnitude (∼2.95 fN/mW) is of the same order as the total achiral force (∼5.59 − 5.03 = 0.56 fN/mW), resulting in the total force along the x–axis changing sign for opposite enantiomers over the top of the waveguide, thus, pushing enantiomers to opposite sides along the x–direction. The motion of 500 particles per enantiomer is tracked individually for 2 s given the total optical force field shown in Fig. 3. The microchannel dimensions (width × height) are 3 μm × 0.35 μm. The resulting final positions of the particles are plotted in Fig. 3 for both enantiomers. From among the 500 (+)-particles 66.2% end up on the left side ($x < 0$) and 65.6% of (−)-particles end up on the right side ($x > 0$), yielding an enantiomer fraction (EF) of 65.8% and 66.0%, respectively. The (+)-EF is calculated within the region $x < 0$ and the (−)-EF is calculated within the region $x > 0$.

A way to increase the strength of chiral forces over the achiral forces is by exploiting the wavelength dependency of the forces. Some of the forces depend on the ratio r/λ, as previously discussed for Eq. (6). This dependency is studied in Fig. 2(c) for the quasi-TE mode, where the total chiral and achiral forces along x–direction, which is the sorting direction, are represented with respect to the particle radius for three wavelengths (405 nm, 780 nm, and 1310 nm). The calculated forces are expected to be more accurate for particles whose size is smaller than the wavelength: $2r < \lambda/n_{water}$ due to the dipolar approximation assumption [38]. This upper bound is ∼150 nm, 290 nm, and 490 nm for $\lambda = 405$ nm, 780 nm, and 1310 nm, respectively. In all the cases, the forces are evaluated at a point positioned at a vertical distance equal to the particle's radius over the top of the waveguide and at a horizontal

distance equal to 1/4 of the waveguide's width from the center, as shown in the inset in Fig. 2(e). That vertical distance is the minimum distance the particle can be placed due to its size. Figure 2(c) shows that there is a particle size range over which chiral forces become larger than achiral forces along the x–direction: 65–132 nm for $\lambda = 405$ nm, 123–257 nm for $\lambda = 780$ nm, and 204–378 nm for $\lambda = 1310$ nm. In fact, there is a specific radius that maximizes the ratio of chiral force over achiral force within those intervals. In these ranges, the spin magnetic force is stronger than the other achiral forces along the x–direction. However, for smaller radii, the achiral magnetic gradient becomes dominant, and for larger radii, the sum of the achiral flow force due to the imaginary part of the Poynting vector and the achiral magnetic gradient becomes dominant instead. In addition, these intervals suggest that operating at shorter wavelengths is more suitable for sorting smaller chiral particles.

Another way to facilitate the horizontal chiral separation is to lower the strength of the achiral gradient forces along the x–axis. This can be achieved by making the waveguide wider. The power is thus spread over a larger area, thereby reducing the gradient of the fields and their respective achiral gradient forces along the x–axis. In addition, the smallest particle size for which chiral and achiral forces have the same magnitude reduces down to 28 nm for $\lambda = 405$ nm. This comes at the expense of reducing the strength of the chiral optical force too (∼0.469 fN/mW), as shown in Fig. 4 for a waveguide 2.27 μm wide × 0.139 μm thick, since the power of the mode has been distributed over a larger cross-section. The particle tracking simulation inside a microchannel of the same dimensions as before (3 μm wide × 0.35 μm thick) yielded values of EF of 60.6%/60.2% for the (+)/(−)-enantiomers, which are somewhat smaller when compared with the narrower waveguide despite the magnitude of the forces being one order of magnitude less. This might be because the wider waveguide allows the interaction between the particle and optical force for a longer time because the waveguide width is larger. In spite of yielding similar enantiomeric separation capability, this wider configuration should be easier to implement experimentally due to the larger area of interaction between the mode and the particles.

B. Quasi-CP Mode

We refer to the quasi-CP mode as a guided mode that is obtained by the superposition of the TE_0 mode and the TM_0 mode delayed by a phase shift of 90°. As the electric field is predominantly horizontally polarized in the TE_0 mode and predominantly vertically polarized in the TM_0 mode, the combination originates a guided mode with an effective circular polarization and, therefore, local helicity [16]. The waveguide width and thickness are chosen so that the TE_0 mode and the TM_0 mode are degenerate, i.e., both modes exhibit the same effective refractive index ($\Delta n = n_{TE} - n_{TM} = 0$) at the target wavelength. This degeneracy allows the circular polarization of the mode to be maintained along the waveguide.

We compute the dominant achiral and chiral forces of this system for a particle of 52 nm radius and a wavelength of 1310 nm (see Fig. 5). The field of the quasi-CP mode exhibits an intrinsic local helicity $\mathfrak{G}$, which naturally diminishes along
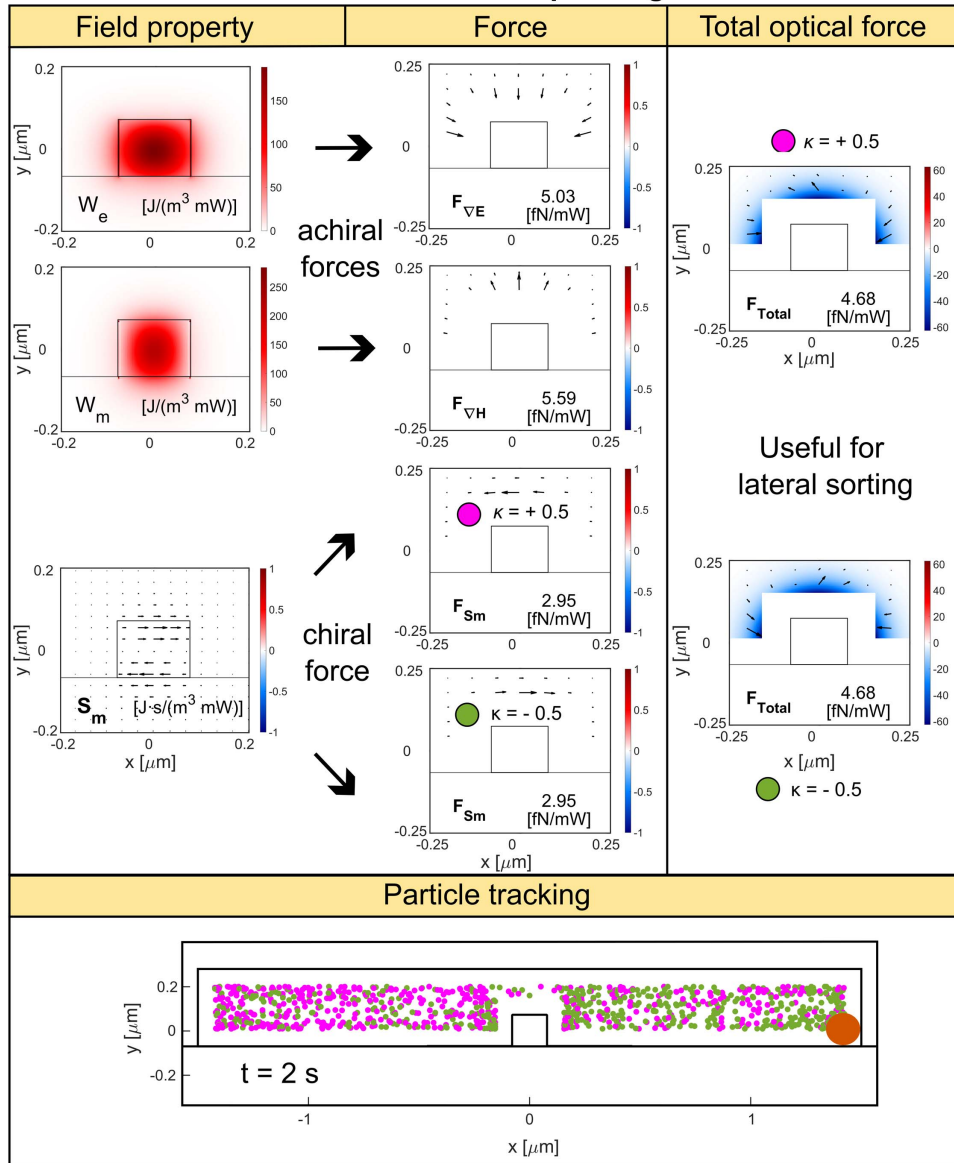
Fig. 3. Field properties (W_e, W_m, and S_m) that generate the dominant forces of the quasi-TE mode in a strip waveguide (0.151 μm wide × 0.139 μm thick) at $\lambda = 405$ nm. The force stemming from the S_m as well as the total optical force is represented for both chiralities of the particle ($\kappa = \pm 0.5$). All forces are calculated for a particle of 80 nm radius. The axes of all graphs refer to the x– and y–coordinates measured in μm units. The arrow map represents the transversal components of the vectorial quantities being plotted, and the colormap represents the scalar quantity or the z–component of the vectorial quantity being plotted. The particle tracking graph shows the last position of 500 particles per enantiomer inside the microchannel (3 μm wide × 0.35 μm thick) after 2 s of motion given the total optical force field produced by the waveguide. The initial x–coordinate of each particle was uniformly randomized between –0.5 and 0.5 μm, and the initial y–coordinate was uniformly randomized with any value within the microchannel. The orange circle represents the particle size to scale, whereas the magenta and green dots represent the center of mass of the enantiomeric particles.

the evanescent field beyond the waveguide core. This is a robust way of achieving a helicity gradient, which is in fact the predominant chiral force in this system. This force is particularly interesting because it depends only on the chiral polarizability, which means that it grows with the radius of the particle as r^3 instead of r^6, and does not depend explicitly on the wavelength. The total optical force exhibits opposite directions for opposite

chiralities, being attractive towards the waveguide for the (+)-particles (with value ~3.29 fN/mW) and repulsive for the (–)-particles (with value ~2.69 fN/mW).

In order to identify the possible range of sizes that might be easier to sort with the quasi-CP compound mode, we performed the study of the chiral force's dependence on the particle's size at the wavelength of 1310 nm. As shown in Fig. 2(d),
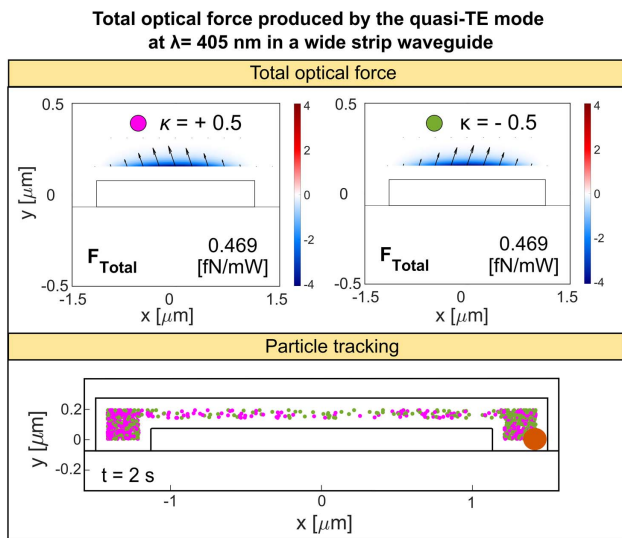
**Total optical force produced by the quasi-TE mode
at λ= 405 nm in a wide strip waveguide**

Fig. 4. Total optical force (transversal in arrow map, and longitudinal in colormap) that a quasi-TE mode in a wide strip waveguide (2.270 μm wide × 0.139 μm thick) at $\lambda = 405$ nm exerts on an 80 nm radius particle is shown for both chiralities of particle $\kappa \pm 0.5$. The particle tracking graph shows the last position of 500 particles per enantiomer inside the microchannel (3 μm wide × 0.35 μm thick) after 2 s of motion given the total optical force field shown in the same figure. The initial x–coordinate of each particle was uniformly randomized between –0.5 and 0.5 μm, and the initial y–coordinate was uniformly randomized with any value within the microchannel. The orange circle represents the particle size to scale, whereas the magenta and green dots represent the center of mass of the enantiomeric particles.

the net transversal chiral force (along x– and y–axis) dominates the net transversal achiral force, up to a maximum size (378 nm) where the combination of the forces due to the real and imaginary parts of the Poynting vector and the rotational of the spin overtake the helicity gradient force. Crucially, this means that the size range has no minimum radii where the chiral force is smaller than the achiral force, as it occurs for the quasi-TE mode. This means that we can expect to reach enantioseparation for smaller particles when compared to the TE mode, even down to radii around 1 nm (molecular size), making this force the most promising for sorting molecules. The particle tracking results inside a microchannel (1.5 μm wide × 1 μm thick) for the system in Fig. 5 show that 33.2% of the 500 (+)-particles become "attached" to the waveguide within a radius of 425 nm measured from the center of the waveguide, and that 90.2% of the 500 (–)-particles are repelled. The (+)-EF within a radius of 425 nm is 77.2% and the (–)-EF outside the radius of 425 nm is 57.5%. Particle tracking simulations assuming optical power above 20 mW, and therefore stronger forces, suggest that the (+)-EF and (–)-EF increase with power injected into the mode yielding 94.5% and 77.9% for 50 mW and 99.6% and 97.3% for 100 mW.

Enantioseparating forces depend on the chirality parameter κ, as shown in Eq. (6), which we have considered to be $\kappa = \pm 0.5$. However, the chiral parameter might be much lower for realistic particles such as molecules. We have computed the modulus of the chiral and achiral forces depending on κ for both the

quasi-TE [Fig. 6(a)] and quasi-CP [Fig. 6(b)] modes. The results suggest that particles with $\kappa > 0.21$ ($\kappa > 0.19$) can be sorted under quasi-TE (quasi-CP) mode operation. Other configurations are needed to achieve the separation of particles with lower chirality. This will be explored in future work.

6. CONCLUSIONS

In conclusion, we have identified an opportunity for transversal enantioseparation via optical forces in photonic integrated waveguides of high-chirality particles utilizing distinct mechanisms depending on particle size and operating wavelength. To this end, we have used the most straightforward waveguide structure: a strip SiN waveguide placed on a silica substrate. At short wavelengths (405 nm), the spin magnetic force arising from a quasi-TE mode is strong enough to sort particles of 80 nm radius in less than 2 s. At longer wavelengths (1310 nm), the helicity gradient force stemming from a quasi-CP mode can separate particles of radius as small as 52 nm radius under time spans below 2 s. In contrast to other approaches using optical waveguides [17–19], our waveguides are longitudinally invariant, meaning that the optical chiral forces could be exerted over long distances (cm-scale), thus facilitating practical enantioseparation with realistic optical powers in the chip (20 mW). These findings highlight the potential of optical forces generated in integrated waveguides in facilitating enantioseparation within the specified parameters of high chirality, particle size, and wavelength.

APPENDIX A: PARTICLE TRACKING ALGORITHM

The motion for a Brownian particle immersed in a fluid and subjected to a (optical) force field $\boldsymbol{F} = (F_x, F_y, F_z)$ is governed by the Langevin equation [39]

$$m\frac{\mathrm{d}^2\boldsymbol{x}}{\mathrm{d}t^2} = \underbrace{-\gamma\frac{\mathrm{d}\boldsymbol{x}}{\mathrm{d}t}}_{\text{friction}} + \underbrace{\boldsymbol{F}}_{\text{optical}} + \underbrace{\gamma\sqrt{2D}\boldsymbol{\xi}(t)}_{\text{stochastic}}. \quad \textbf{(A1)}$$

This equation can be integrated by iteratively calculating the displacements over successive time intervals Δt. If the time step is larger than the momentum relaxation time $\tau = m/\gamma$, i.e., $\Delta t \gg \tau$, the previous equation simplifies to the so-called overdamped Langevin equation [30,39]

$$0 = -\gamma\frac{\mathrm{d}\boldsymbol{x}}{\mathrm{d}t} + \boldsymbol{F} + \gamma\sqrt{2D}\boldsymbol{\xi}(t), \quad \textbf{(A2)}$$

whose solution can be given by the Euler-Maruyama integration scheme [31,32] to track the location of the particle in time:

$$x^{(m+1)} = x^{(m)} + \mathcal{M}_{x,\perp}^{(m)}F_x^{(m)}\Delta t + \sqrt{2\mathcal{M}_{x,\perp}^{(m)}k_BT\Delta t}\, N_x(0,1),$$

$$y^{(m+1)} = y^{(m)} + \mathcal{M}_{y,\perp}^{(m)}F_y^{(m)}\Delta t + \sqrt{2\mathcal{M}_{y,\perp}^{(m)}k_BT\Delta t}\, N_y(0,1),$$

$$z^{(m+1)} = z^{(m)} + \mathcal{M}_{z,||}^{(m)}F_z^{(m)}\Delta t + \sqrt{2\mathcal{M}_{z,||}^{(m)}k_BT\Delta t}\, N_z(0,1),$$
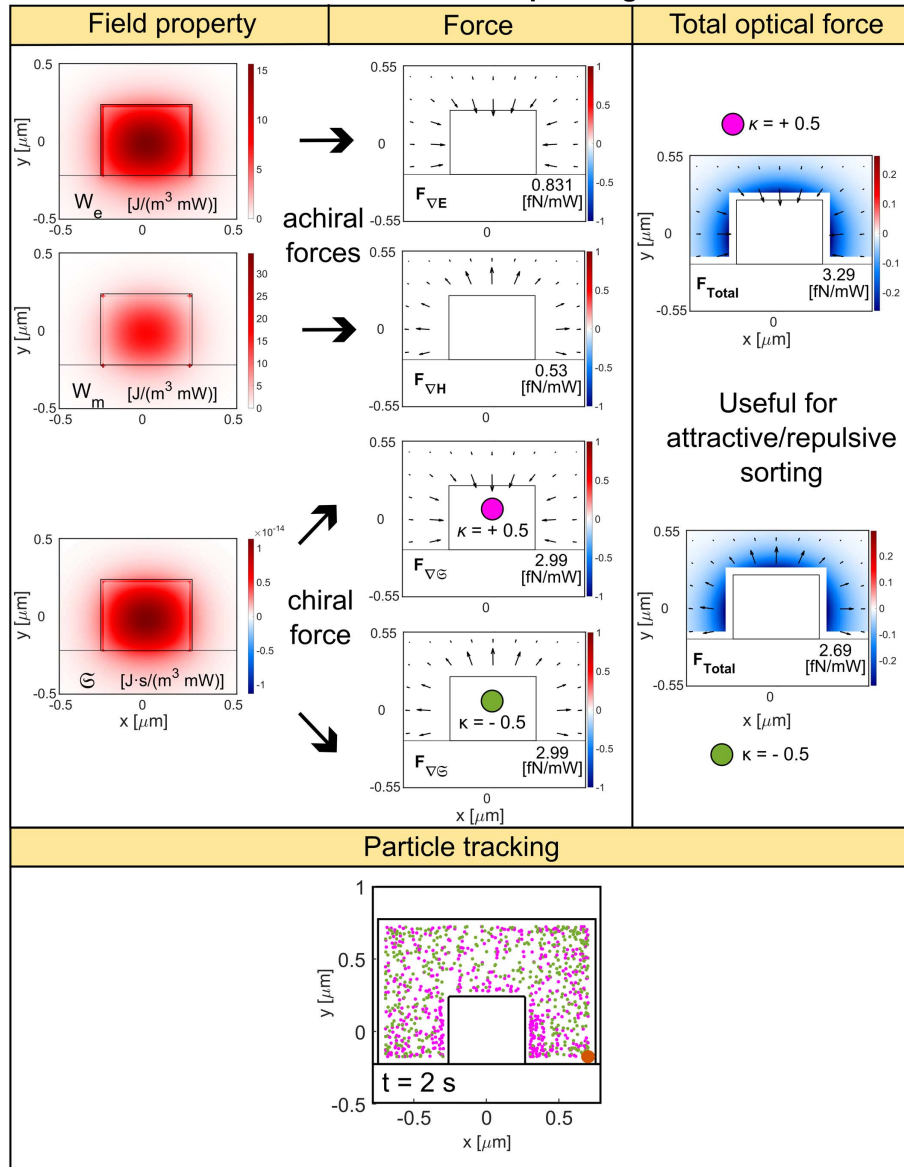
$$\textbf{(A3)}$$

Fig. 5. Field properties (W_e, W_m and $\mathcal{G}$) that generate the dominant forces of the quasi-CP mode in a strip waveguide (0.495 μm wide × 0.450 μm thick). The force stemming from the gradient of $\mathcal{G}$ as well as the total force is represented for both chiralities of the particle ($\kappa = \pm 0.5$). All forces are calculated for a particle of 52 nm radius. The arrow map represents the transversal components of the vectorial quantities being plotted, and the colormap represents the scalar quantity or the z–component of the vectorial quantity being plotted. The particle tracking graph shows the last position of 500 particles per enantiomer inside the microchannel (1.5 μm wide × 1 μm thick) after 2 s of motion given the total optical force field produced by the waveguide. The initial x–coordinate of each particle was uniformly randomized between −0.5 and 0.5 μm, and the initial y–coordinate was uniformly randomized with any value within the microchannel. The orange circle represents the particle size to scale, whereas the magenta and green dots represent the center of mass of the enantiomeric particles.

where $N(0,1)$ represents a standard normal distribution with 0–mean and 1–variance, and the force field $\boldsymbol{F}$ is evaluated at the location of the particle $(x^{(m)}, y^{(m)}, z^{(m)})$ at each instant of time. The time step used in all our particle tracking simulations is $\Delta t = 10$ μs. Let us compare this value with the momentum relaxation time for a material with a similar permittivity to the one considered in the main text for the particles, SiO$_2$ ($\rho_{\text{SiO}_2} = 2650$ kg/m³, $\varepsilon_p \sim 2$), within the size range considered in this work ($r \sim 80$ nm):

$$\Delta t \gg \tau = \frac{m}{\gamma} = \frac{\rho_{\text{SiO}_2} \frac{4}{3}\pi r^3}{6\pi\eta r} = \frac{2\rho_{\text{SiO}_2} r^2}{9\eta} \sim 2.4 \text{ ns.} \quad \textbf{(A4)}$$

Our choice of $\Delta t = 10$ μs $\gg 2.4$ ns fulfils this requirement. The mass of the particles is so small that in practice, one can consider that they lack inertia and the velocity is constant over Δt. The upper bound on the time step is chosen so that the particle moves one-pixel distance as maximum. In our case, the spatial resolution was $\Delta x_{\min} = 10$ nm, and the

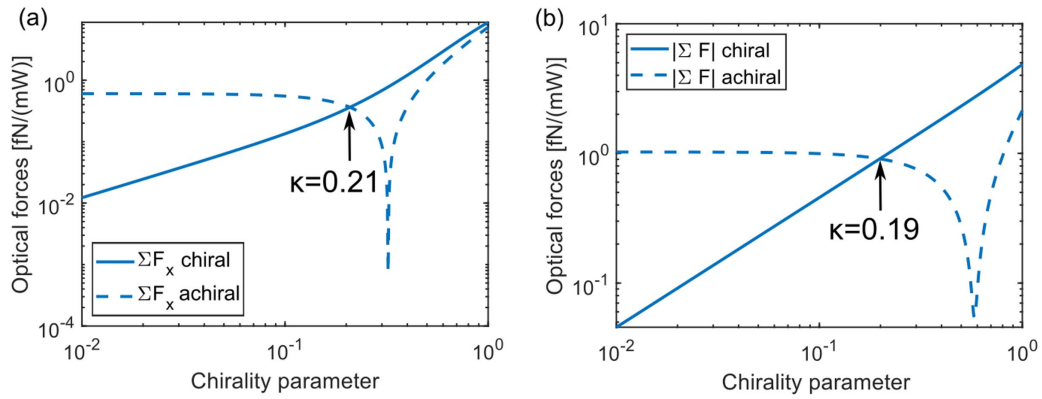**Fig. 6.** Net chiral and achiral forces exerted on a particle depending on its chirality parameter κ for (a) quasi-TE mode ($\lambda = 405$ nm) along the x–direction and particle size $r = 80$ nm and (b) quasi-CP mode ($\lambda = 1310$ nm) and particle size of $r = 52$ nm. The limit where the achiral force becomes stronger than the chiral force is at $\kappa = 0.21$ for the quasi-TE mode and $\kappa = 0.19$ for the quasi-CP mode. The forces were evaluated in the same position as in Figs. 2(c) and 2(d).

maximum value of the force for the quasi-TE mode was 93 fN (20 mW) for an 80 nm particle; therefore, this upper bound is

$$\Delta t \ll \frac{\Delta x_{\min}\gamma}{\max|F|} \sim 162 \; \mu\text{s}, \tag{A5}$$

which is also fulfilled by our choice of time step. An identical argument would follow for the quasi-CP mode.

The mobility coefficients are modified from the bulk value $\mathcal{M}$ to account for the hydrodynamic interaction between the particle and the enclosing boundaries. The modifications are different depending on whether the particle moves along the directions parallel (||) or perpendicular ($\perp$) to a non-slip planar boundary [33]:

$$\mathcal{M}_{\perp}(h) = \mathcal{M}\left(1 - \frac{9}{8}\left(\frac{r}{h}\right) + \frac{1}{2}\left(\frac{r}{h}\right)^3 - \frac{1}{8}\left(\frac{r}{h}\right)^5\right),$$

$$\mathcal{M}_{||}(h) = \mathcal{M}\left(1 - \frac{9}{16}\left(\frac{r}{h}\right) + \frac{1}{8}\left(\frac{r}{h}\right)^3 - \frac{1}{16}\left(\frac{r}{h}\right)^5\right), \tag{A6}$$

where h is the distance from the center of the particle to the wall, and r is the radius of the spherical particle. We used the $\perp$–correction for the x– and y–directions and the ||–correction for the z–direction. We do not allow the particles to come closer than a radius distance from the wall, i.e., $h \geq r$. This bounds the values of r/h between zero and one, and therefore, $\mathcal{M}_{\perp} \in [\mathcal{M}/4, \mathcal{M}]$, $\mathcal{M}_{||} \in [\mathcal{M}/2, \mathcal{M}]$. These modified coefficients are obtained for the case of a particle moving near a single planar boundary. However, in our waveguide system, we have multiple boundaries, defined by the ceiling and sidewalls of the microchannel as well as the top and sidewalls of the waveguide core and top of the substrate. We assume the modified expressions are still valid. We use the $\mathcal{M}_{\perp}$ expression for calculating the mobility coefficient along x– and y–directions, and use the $\mathcal{M}_{||}$ expression along z–direction. We take h as the distance to the nearest boundary in the direction of motion. For instance, for the calculation of $\mathcal{M}_{y,\perp}$ we compute h by measuring the distance from the particle position to the ceiling of the microchannel and compare it to the distance to the substrate or top of the waveguide core (depending on whether the particle's position is above the substrate or above the waveguide core). Whichever distance is shorter, that is the value of h.

The force field used in the algorithm is obtained for a system that is not enclosed by a microchannel. However, we assume the presence of the microchannel does not modify the guided modes, and thus, the force field produced by the waveguide throughout the surrounding medium (water, $n = 1.33$). This approximation is valid due to the higher refractive index of the waveguide core (SiN, $n \sim 2$) with respect to that of the microchannel material (SiO$_2$, $n \sim 1.45$), which ensures the guidance of the mode along the core, and because the microchannel walls (boundaries) are separated by a distance $\geq \lambda/1.33$ from the waveguide walls.

Once the particle tracking simulation is finished, we do statistical analysis with the last positions of the 500 particles for both enantiomers, to compute the enantiomer fraction. Given the number of (+)-particles, N_+, and the number of (−)-particles, N_-, inside a region of space, we define the enantiomer fraction (EF) as [40]

$$(+)\text{-EF} = \frac{N_+}{N_+ + N_-}, \quad (-)\text{-EF} = \frac{N_-}{N_+ + N_-}. \tag{A7}$$

Since the chiral forces separate opposite enantiomers in opposite directions, the (+)-EF and the (−)-EF are calculated in different regions of space. For instance, for the quasi-TE mode, the (+)-EF is calculated for the region $x < 0$, whereas the (−)-EF is obtained for the region $x > 0$. And, for the quasi-CP mode, the (+)-EF is calculated for the region $x^2 + y^2 < R^2$ whereas the (−)-EF is obtained for $x^2 + y^2 > R^2$, where R is an arbitrary radius that defines a circular region from the center of the waveguide.

APPENDIX B: SORTING TIME FOR A CLOUD OF ENANTIOMERS IN A FLUID

We derive the expression for calculating the time needed for a chiral optical force, F, to separate two clouds of opposite enantiomers with a distance Δx. This has been previously done by Kravets *et al.* [28], but we include it here for completeness. The chiral force (uniform in space and constant in time) moves each

enantiomer cloud into opposite directions a distance d_{opt} from their initial position,

$$d_{opt} = \frac{F}{\gamma} t, \qquad (B1)$$

where γ is the friction coefficient of the particle motion in the fluid. Let us assume the chiral force moves the (+)-enantiomer

cloud towards the left ($-x$ direction) and the (−)-enantiomer cloud towards the right ($+x$ direction), following the Fig. 1(a) schematic. Therefore, the separation between the center of mass of both clouds has increased $2d_{opt}$. In addition to this displacement, the radius for each enantiomer cloud is expected to increase on average an extra distance d_B from its initial extension $L_0/2$ due to Brownian motion:
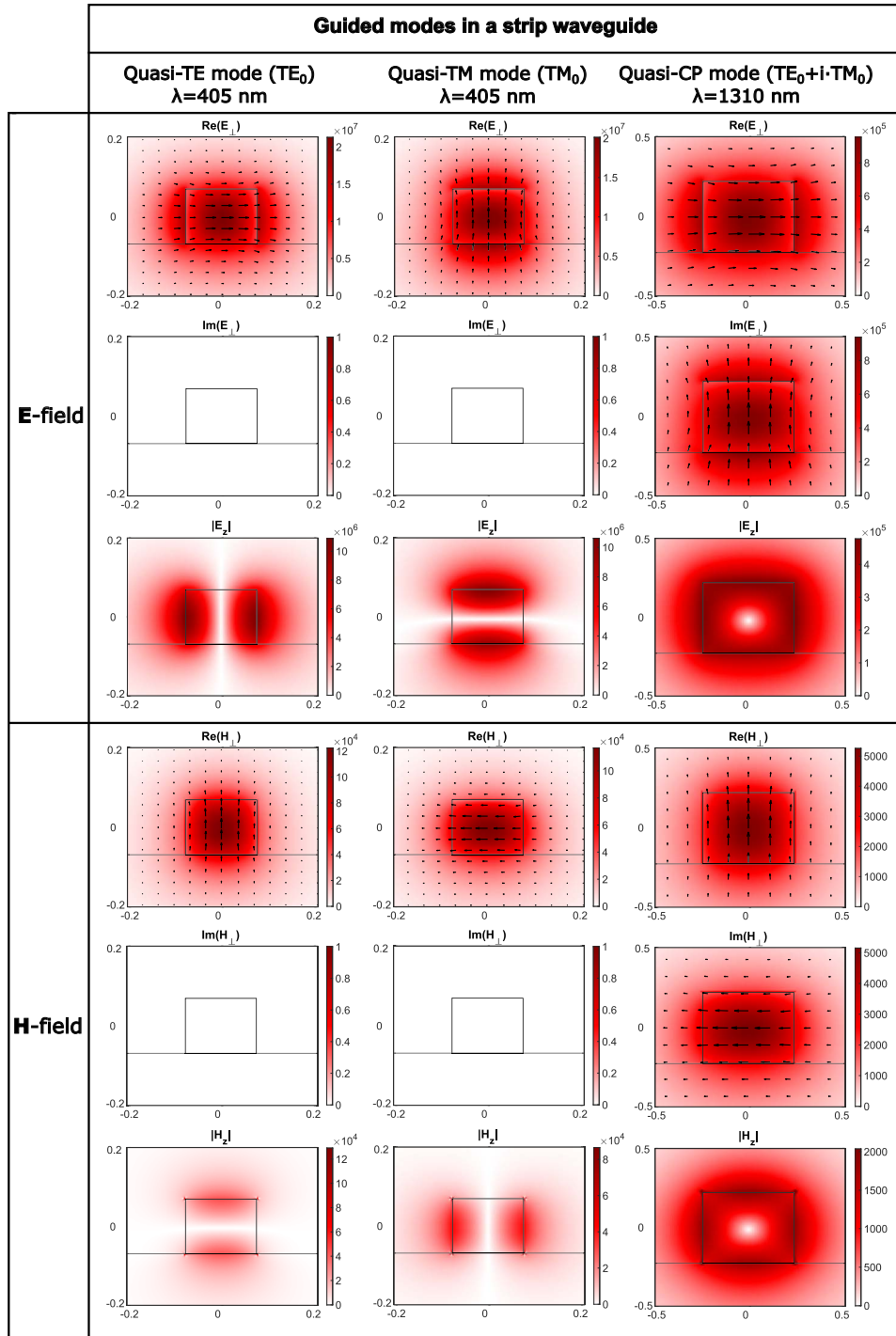

Fig. 7. Electric and magnetic field patterns of the guided modes discussed in the main text for a strip waveguide. The fields are split into the transversal ($\perp$) and longitudinal (z) components. The transversal components of the TE_0 and TM_0 modes lack an imaginary part, whereas the quasi-CP mode does due to the circular polarization of the mode induced by the phase delay of 90°.

$$d_B = \sqrt{2Dt}, \tag{B2}$$

where $D = k_B T/\gamma$ is the diffusion coefficient, k_B is the Boltzmann constant, and T is the absolute temperature of the fluid. These two simultaneous processes of motion are schematized in Fig. 1, where by comparing the defined lengths one can see that the condition to achieve a separation of Δx in a sorting time t is given by

$$2d_{\text{opt}} = L_0 + 2d_B + \Delta x, \tag{B3}$$

$$2\frac{F}{\gamma}t = L_0 + 2\sqrt{2D}\sqrt{t} + \Delta x. \tag{B4}$$

This equation can be solved as a second-degree equation on the variable $\sqrt{t}$, whose solution is

$$\sqrt{t_{\text{sort}}} = \frac{\gamma}{F}\sqrt{\frac{D}{2}}\left(1 + \sqrt{1 + \frac{F(L_0 + \Delta x)}{D\gamma}}\right), \tag{B5}$$

where we have taken the positive square root solution for avoiding unphysical negative time. By squaring this last expression and substituting $D = k_B T/\gamma$ and $\gamma = 6\pi\eta r$, the sorting time can be obtained:

$$t_{\text{sort}} = 3\pi\eta k_B T \frac{r}{F^2}\left(1 + \sqrt{1 + \frac{F(L_0 + \Delta x)}{k_B T}}\right)^2. \tag{B6}$$

Note that no dipolar approximation is needed to derive this equation since we do not require the expression of the force.

APPENDIX C: ELECTRIC AND MAGNETIC FIELDS OF THE GUIDED MODES

The decomposition of the electric and magnetic fields for the quasi-TE, quasi-TM, and quasi-CP modes can be found in Fig. 7.

REFERENCES

1. J. Jacques, A. Collet, and S. H. Wilen, *Enantiomers, Racemates and Resolutions* (Wiley, 1981).
2. C. Genet, "Chiral light–chiral matter interactions: an optical force perspective," ACS Photonics **9**, 319–332 (2022).
3. Y. Zhao, A. A. E. Saleh, M. A. van de Haar, *et al.*, "Nanoscopic control and quantification of enantioselective optical forces," Nat. Nanotechnol. **12**, 1055–1059 (2017).
4. A. Canaguier-Durand, J. A. Hutchison, C. Genet, *et al.*, "Mechanical separation of chiral dipoles by chiral light," New J. Phys. **15**, 123037 (2013).
5. A. Hayat, J. P. B. Mueller, and F. Capasso, "Lateral chirality-sorting optical forces," Proc. Natl. Acad. Sci. USA **112**, 13190–13194 (2015).
6. A. Canaguier-Durand and C. Genet, "Chiral route to pulling optical forces and left-handed optical torques," Phys. Rev. A **92**, 043823 (2015).
7. T. Zhang, M. R. C. Mahdy, Y. Liu, *et al.*, "All-optical chirality-sensitive sorting via reversible lateral forces in interference fields," ACS Nano **11**, 4292–4300 (2017).
8. T. Cao, L. Mao, Y. Qiu, *et al.*, "Fano resonance in asymmetric plasmonic nanostructure: separation of sub-10 nm enantiomers," Adv. Opt. Mater. **7**, 1801172 (2019).
9. H. Zheng, X. Li, J. Ng, *et al.*, "Tailoring the gradient and scattering forces for longitudinal sorting of generic-size chiral particles," Opt. Lett. **45**, 4515–4518 (2020).
10. Z. Zhang, C. Min, Y. Fu, *et al.*, "Controllable transport of nanoparticles along waveguides by spin-orbit coupling of light," Opt. Express **29**, 6282–6292 (2021).
11. G. Tkachenko and E. Brasselet, "Optofluidic sorting of material chirality by chiral light," Nat. Commun. **5**, 3577 (2014).
12. H. Magallanes and E. Brasselet, "Macroscopic direct observation of optical spin-dependent lateral forces and left-handed torques," Nat. Photonics **12**, 461–464 (2018).
13. Y. Shi, T. Zhu, T. Zhang, *et al.*, "Chirality-assisted lateral momentum transfer for bidirectional enantioselective separation," Light Sci. Appl. **9**, 62 (2020).
14. S. Golat, J. J. Kingsley-Smith, I. Díez, *et al.*, "Optical chiral sorting forces and their manifestation in evanescent waves and nanofibres," arXiv, arXiv:2310.11272 (2023).
15. A. Espinosa-Soria and A. Martínez, "Transverse spin and spin-orbit coupling in silicon waveguides," IEEE Photonics Technol. Lett. **28**, 1561–1564 (2016).
16. J. E. Vázquez-Lozano and A. Martínez, "Toward chiral sensing and spectroscopy enabled by all-dielectric integrated photonic waveguides," Laser Photonics Rev. **14**, 1900422 (2020).
17. L. Fang and J. Wang, "Optical trapping separation of chiral nanoparticles by subwavelength slot waveguides," Phys. Rev. Lett. **127**, 233902 (2021).
18. Y. Liu, W. Zhang, L. He, *et al.*, "All-optical separation of chiral nanoparticles on silicon-based microfluidic chips with vector exceptional points," APL Photonics **8**, 036112 (2023).
19. L. Fang and J. Wang, "Extraordinary coupled spin and chirality of electromagnetic guided waves," arXiv, arXiv:2304.04764 (2023).
20. C. Xiang, W. Jin, and J. E. Bowers, "Silicon nitride passive and active photonic integrated circuits: trends and prospects," Photonics Res. **10**, A82–A96 (2022).
21. P. C. Chaumet and A. Rahmani, "Electromagnetic force and torque on magnetic and negative-index scatterers," Opt. Express **17**, 2224–2234 (2009).
22. M. Nieto-Vesperinas, J. J. Sáenz, R. Gómez-Medina, *et al.*, "Optical forces on small magnetodielectric particles," Opt. Express **18**, 11428–11443 (2010).
23. P. A. Belov, S. I. Maslovski, K. R. Simovski, *et al.*, "A condition imposed on the electromagnetic polarizability of a bianisotropic lossless scatterer," Tech. Phys. Lett. **29**, 718–720 (2003).
24. I. Sersic, C. Tuambilangana, T. Kampfrath, *et al.*, "Magnetoelectric point scattering theory for metamaterial scatterers," Phys. Rev. B **83**, 245102 (2011).
25. J. Mun, M. Kim, Y. Yang, *et al.*, "Electromagnetic chirality: from fundamentals to nontraditional chiroptical phenomena," Light Sci. Appl. **9**, 139 (2020).
26. H. Chen, C. Liang, S. Liu, *et al.*, "Chirality sorting using two-wave-interference–induced lateral optical force," Phys. Rev. A **93**, 053833 (2016).
27. S. Wang and C. Chan, "Lateral optical force on chiral particles near a surface," Nat. Commun. **5**, 3307 (2014).
28. N. Kravets, A. Aleksanyan, H. Chraïbi, *et al.*, "Optical enantioseparation of racemic emulsions of chiral microparticles," Phys. Rev. Appl. **11**, 044025 (2019).

29. G. Schnoering, S. Albert, A. Canaguier-Durand, *et al.*, "Chiral thermodynamics in tailored chiral optical environments," Phys. Rev. X **11**, 041022 (2021).

30. T. Horai, H. Eguchi, T. Iida, *et al.*, "Formulation of resonant optical force based on the microscopic structure of chiral molecules," Opt. Express **29**, 38824–38840 (2021).

31. P. E. Kloeden and E. Platen, *Numerical Solution of Stochastic Differential Equations* (Springer-Berlin, 1992).

32. S. Kieninger and B. G. Keller, "Path probability ratios for Langevin dynamics—exact and approximate," J. Chem. Phys. **154**, 094102 (2021).

33. J. W. Swan and J. F. Brady, "Simulation of hydrodynamically interacting particles near a no-slip boundary," Phys. Fluids **19**, 113306 (2007).

34. J. B. Knight, A. Vishwanath, J. P. Brody, *et al.*, "Hydrodynamic focusing on a silicon chip: mixing nanoliters in microseconds," Phys. Rev. Lett. **80**, 3863–3866 (1998).

35. L. Castelló-Pedrero, M. I. Gómez-Gómez, J. García-Rupérez, *et al.*, "Performance improvement of a silicon nitride ring resonator biosensor operated in the tm mode at 1310 nm," Biomed. Opt. Express **12**, 7244–7260 (2021).

36. M. Li, S. Yan, Y. Zhang, *et al.*, "Optical separation and discrimination of chiral particles by vector beams with orbital angular momentum," Nanoscale Adv. **3**, 6897–6902 (2021).

37. K. Y. Bliokh, D. Smirnova, and F. Nori, "Quantum spin hall effect of light," Science **348**, 1448–1451 (2015).

38. J. R. Arias-González and M. Nieto-Vesperinas, "Optical forces on small particles: attractive and repulsive nature and plasmon-resonance conditions," J. Opt. Soc. Am. A **20**, 1201–1209 (2003).

39. D. L. Ermak and J. A. McCammon, "Brownian dynamics with hydrodynamic interactions," J. Chem. Phys. **69**, 1352–1360 (1978).

40. S. W. Smith, "Chiral toxicology: it's the same thing…only different," Toxicol. Sci. **110**, 4–30 (2009).